

Atomic-Scale Visualization of Quasiparticle Interference on a Type-II Weyl Semimetal Surface

Hao Zheng,¹ Guang Bian,¹ Guoqing Chang,^{2,3} Hong Lu,⁴ Su-Yang Xu,¹ Guangqiang Wang,⁴ Tay-Rong Chang,⁵ Songtian Zhang,¹ Ilya Belopolski,¹ Nasser Alidoust,¹ Daniel S. Sanchez,¹ Fengqi Song,⁶ Horng-Tay Jeng,^{5,7}

Nan Yao,⁸ Arun Bansil,⁹ Shuang Jia,^{4,10} Hsin Lin,^{2,3} and M. Zahid Hasan^{1,*}

¹Laboratory for Topological Quantum Matter and Spectroscopy (B7), Department of Physics, Princeton University, Princeton, New Jersey 08544, USA

²Centre for Advanced 2D Materials and Graphene Research Centre, National University of Singapore, 6 Science Drive 2, Singapore 117546, Singapore

³Department of Physics, National University of Singapore, 2 Science Drive 3, Singapore 117542, Singapore

⁴International Center for Quantum Materials, School of Physics, Peking University, Beijing 100871, China

⁵Department of Physics, National Tsing Hua University, Hsinchu 30013, Taiwan

⁶National Laboratory of Solid State Microstructures, Collaborative Innovation Center of Advanced Microstructures and Department of Physics, Nanjing University, Nanjing 210093, China

⁷Institute of Physics, Academia Sinica, Taipei 11529, Taiwan

⁸Princeton Institute for the Science and Technology of Materials, Princeton University, 70 Prospect Avenue, Princeton, New Jersey 08540, USA

⁹Department of Physics, Northeastern University, Boston, Massachusetts 02115, USA

¹⁰Collaborative Innovation Center of Quantum Matter, Beijing 100871, China

(Received 8 September 2016; revised manuscript received 16 November 2016; published 23 December 2016)

We combine quasiparticle interference simulation (theory) and atomic resolution scanning tunneling spectromicroscopy (experiment) to visualize the interference patterns on a type-II Weyl semimetal $\text{Mo}_x\text{W}_{1-x}\text{Te}_2$ for the first time. Our simulation based on first-principles band topology theoretically reveals the surface electron scattering behavior. We identify the topological Fermi arc states and reveal the scattering properties of the surface states in $\text{Mo}_{0.66}\text{W}_{0.34}\text{Te}_2$. In addition, our result reveals an experimental signature of the topology via the interconnectivity of bulk and surface states, which is essential for understanding the unusual nature of this material.

DOI: 10.1103/PhysRevLett.117.266804

Recent discovery of type-I Weyl fermions in the TaAs class of materials has generated a flurry of new research directions [1–11]. Many important predictions including Weyl cone, Fermi arc, chiral anomaly effect, and novel quasiparticle interference (QPI) were experimentally observed [10–17]. Very recently, a new type of Weyl quasiparticle was predicted in WTe_2 , MoTe_2 and their alloys [18–21]. The novelty is that this type (type II) of Weyl fermions breaks Lorentz symmetry, and thus cannot exist as a fundamental particle in nature. Such an excitation can emerge in a crystal as low-energy quasiparticles. Theory predicts that type-II Weyl semimetals host a number of unusual effects, e.g., a new type of chiral anomaly, unconventional anomalous Hall effect, and interaction-induced emergent Lorentz invariant properties, which are not possible in type-I Weyl semimetals [22–24]. Thus the experimental investigation of the MoWTe class of materials is desirable.

Scanning tunneling microscopy and spectroscopy (STM–STS) is a vital tool for the investigation and illumination of various key properties of a topological matter [25–29]. The Fermi arc surface state, which is the topological fingerprint of Weyl semimetals, is predicted to exhibit exotic interference behavior in tunneling spectroscopy and

magnetotransport measurements [30–33]. Another unique property of a Weyl semimetal is the topological connection. An electron in a Fermi arc surface state, when it moves to (or is scattered to) the Weyl node, sinks into the bulk and travels to the opposite surface [30]. These features are interesting in connection to their QPI.

We employed low temperature STM–STS to investigate the QPI patterns in $\text{Mo}_x\text{W}_{1-x}\text{Te}_2$. The Fermi arc-derived quantum interference patterns are identified. We also performed comprehensive first-principle band structure calculations and QPI simulations on this material for the first time. Combination of our experimental and theoretical results reveals signatures of the predicted unique topological connection in this material.

Single-crystalline $\text{Mo}_{0.66}\text{W}_{0.34}\text{Te}_2$ samples were grown by chemical vapor transport method. After being cleaved at 79 K, they were transferred *in vacuo* to STM (Unisoku) at 4.6 K. dI/dV signals were acquired through a lock-in technique with a modulation at 5 mV and 1 kHz. Experimental QPI maps were generated by symmetrizing the Fourier transformed dI/dV maps (Fig. S1). First-principle-based tight-binding model simulations were used to obtain the electronic band structure. The alloy

$\text{Mo}_x\text{W}_{1-x}\text{Te}_2$ was calculated by interpolation of the tight-binding model matrix elements of WTe_2 and MoTe_2 [40–42]. The theoretical QPI patterns are the restricted joint density of states, which removes all of the spin-flipping scattering vectors (see more details in the Supplemental Material [34]).

Figures 1(a) and 1(b) present the typical morphology of the cleaved $\text{Mo}_{0.66}\text{W}_{0.34}\text{Te}_2(001)$ surface. There are only four point defects observed on the atomically ordered lattice, which confirms the high quality of our samples. In vicinity to the defect [Figs. 1(c) and 1(d)], we observe a butterflylike protrusion in the empty state image, and a depression area, which breaks the atomic row, in the occupied state. Since $\text{Mo}_x\text{W}_{1-x}\text{Te}_2$ is naturally cleaved at a Te-terminated surface, the point defect is attributed to a Te vacancy. From the high resolution STM image of the occupied state [Fig. 1(e)], which probes the surface anions, we are able to clearly resolve an array of alternating atomic rows of extended (bright) and localized (dimmer) wave functions. The measured lattice constants ($a = 0.35$ nm, $b = 0.63$ nm) are consistent with the Te terminated T_d phase of $\text{Mo}_x\text{W}_{1-x}\text{Te}_2$ [35]. The simulated STM image in Fig. 1(f) reproduces the surface structure of the alternating Te-atom rows. We also calculate the density of state, considering only the top Te layer. A typical dI/dV spectrum in Fig. 1(h) displays finite conductance at zero bias, which indicates the (semi-) metallic behavior of the samples. The measured data agree qualitatively with the simulation, which confirms structural properties of our $\text{Mo}_x\text{W}_{1-x}\text{Te}_2$ sample, a candidate for the type-II Weyl semimetal.

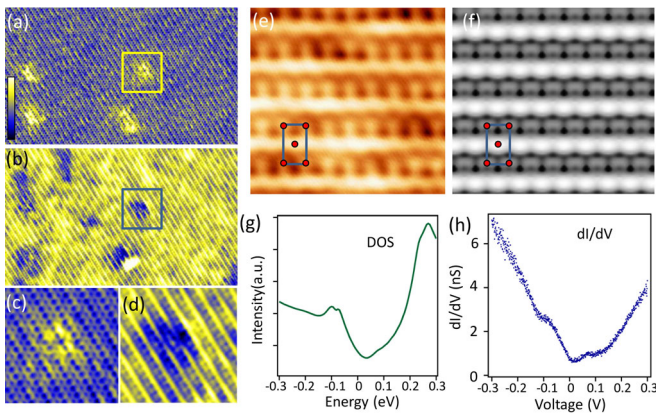


FIG. 1. [(a) and (b)] Large-scale constant-current STM images (30×18 nm²) of the $\text{Mo}_{0.66}\text{W}_{0.34}\text{Te}_2(001)$ surface taken at 100 and -100 mV, respectively. (c) and (d) are the enlarged images (5.3×5.3 nm²) of the defect inside the square in (a) and (b), respectively. (e) and (f) are the atomically resolved experimental and simulated STM images (-100 mV), respectively. In both images, brighter color means higher charge density. Red dots mark the positions of surface Te atoms. The blue rectangles indicate surface unit cells. (g) The calculated density of state. (h) A typical dI/dV spectrum on the $\text{Mo}_{0.66}\text{W}_{0.34}\text{Te}_2$ sample.

As shown in Fig. 2, the type-I Weyl cone consists of well-separated upper and lower branches, and the constant energy contour (CEC) at the energy of the Weyl node is a single point. By contrast, the type-II cone is heavily tilted in k space, leading to the existence of projected bulk pockets (right and left branches of the Weyl cone) on the CEC at the Weyl node energy (and in a large energy range). $\text{Mo}_x\text{W}_{1-x}\text{Te}_2$ is predicted to be a type-II Weyl semimetal [20]. Here, we focus on a $x = 0.66$ sample. We uncover eight Weyl nodes in total. Four are located at 15 meV above the Fermi level (W_1), while the other four nodes sit at 62 meV (W_2). On the CEC at 15 meV [Fig. 2(c)], we find a typical type-II Weyl semimetal feature, the coexistence of projected bulk states and surface states. According to the penetration depth (see more details in Fig. S2), we are able to identify the two bright yellow semicircular contours in Fig. 2(c) as surface states and the remaining light-blue pockets (one bowtie-shaped hole pocket and two elliptical electron pockets) in Fig. 2(c) as projected bulk states. We enlarge the surface state in the vicinity of the two W_1 nodes in Figs. 2(d) and S2, and find that the surface band contour

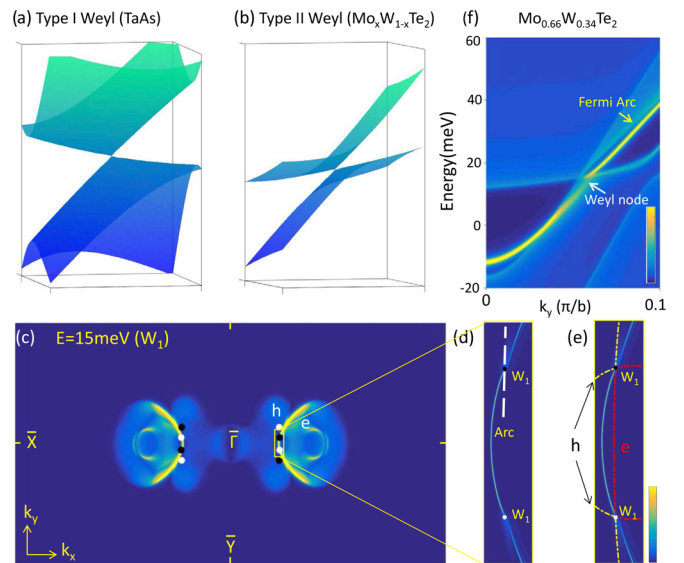


FIG. 2. [(a) and (b)] Schematics of the type-I and the type-II Weyl cone, respectively. (c) The calculated CEC in the first surface Brillouin zone (BZ) of $\text{Mo}_{0.66}\text{W}_{0.34}\text{Te}_2(001)$ at the energy of the Weyl node W_1 . The surface weight of states is indicated by color. Projected Weyl nodes are depicted by dots. The white and black colors stand for the opposite chiralities of the Weyl nodes. e (h) stands for the electron (hole) pocket. [(d) and (e)] The enlarged views of the area inside the yellow rectangle, drawn with a lower color contrast to enhance the visibility of the surface-state contours. The topological Fermi arc, which connects one pair of projected Weyl nodes, is clearly displayed and marked. Yellow and red dotted lines in (e) represent the boundaries of the projected hole and electron bulk pockets. (f) The E - k dispersion cut along the white dashed line in (d). The Weyl node and Fermi arc are marked by white and yellow arrows, respectively.

is split into three segments with tiny gaps in between. The middle segment behaves as a single curve connecting one pair of W_1 nodes and is therefore identified as the Fermi arc. In Fig. 2(e), we plot the edges of the projected bulk bands (the branches of the type-II Weyl cone), and clearly demonstrate that they touch each other at the Weyl nodes. In addition, from the energy-momentum dispersion in Fig. 2(f), one can see the tilted cone in the band structure. Taking these evidences together, we theoretically establish the type-II Weyl state in our $\text{Mo}_{0.66}\text{W}_{0.34}\text{Te}_2$ compound.

We perform dI/dV mapping on the $\text{Mo}_{0.66}\text{W}_{0.34}\text{Te}_2(001)$ surface at various voltages and Fourier transform these maps to gain insight into the QPI information. Figures 3(a)–3(c) exhibit the experimental QPI maps acquired at 50, 100, and 200 meV above Fermi level. The patterns in the red rectangles arise from the intra first BZ quasiparticle scatterings, while patterns close to the Bragg points $(Q_x, Q_y) = [0, \pm(2\pi/b)]$ with weaker intensities arise from the inter-BZ scattering and are replicas of the central features (Fig. S4). For simplicity, we restrict our discussion to the intra-BZ scattering (inside the rectangles) in the rest of this paper. At all energies (Figs. 3 and S5), the experimental QPIs show simple and clean patterns, in contrast to TaAs [14–17]. Specifically, all images consist of only three main pockets: one elliptical pocket in the center and two crescent-shaped contours located on the left and right sides of the central ellipse. The diameters

of the crescents increase with bias voltage, which proves the electronlike (instead of holelike) surface state. We perform model calculations to obtain the theoretical QPI patterns. Figures 3(d)–3(f) produce exactly the same number (three) of QPI pockets at the same locations in Q space, and thus agree well with the experiments. Additionally, the calculated QPI at 100 meV [Fig. 3(e)] remarkably reproduces all dominant features in the measurement [Fig. 3(b)], namely, the central ellipse and the two side crescents. Moreover, the crescent displays a 3 shape rather than a) shape; the weak central feature as marked by the red arrow is also reproduced in the simulation in Fig. 3(e). To further examine the evolution of the QPI features, we study the energy-scattering vector (E - Q) dispersion. In Fig. 3(g) the data in the region between $-\pi/b$ and π/b correspond to the intra-BZ scattering. In this region, the QPI signal displays as a V-shaped dispersion, with the vertex of the V located at $Q = 0$. The linear edges of the V feature marked by white arrows refer to the two cutting points on the crescent pocket, which are indicated by white arrows in Fig. 3(b). Besides this strongly dispersed QPI feature, we also reveal an additional weakly dispersed feature, which is denoted by the red arrow and corresponds to the pocket indicated by the red arrow in Fig. 3(b). The calculated E - Q dispersion reproduces both features in the experimental data in a wide energy range.

Figure 4 shows the QPI map at 50 meV, which is between the energies of W_1 and W_2 . At this energy, the

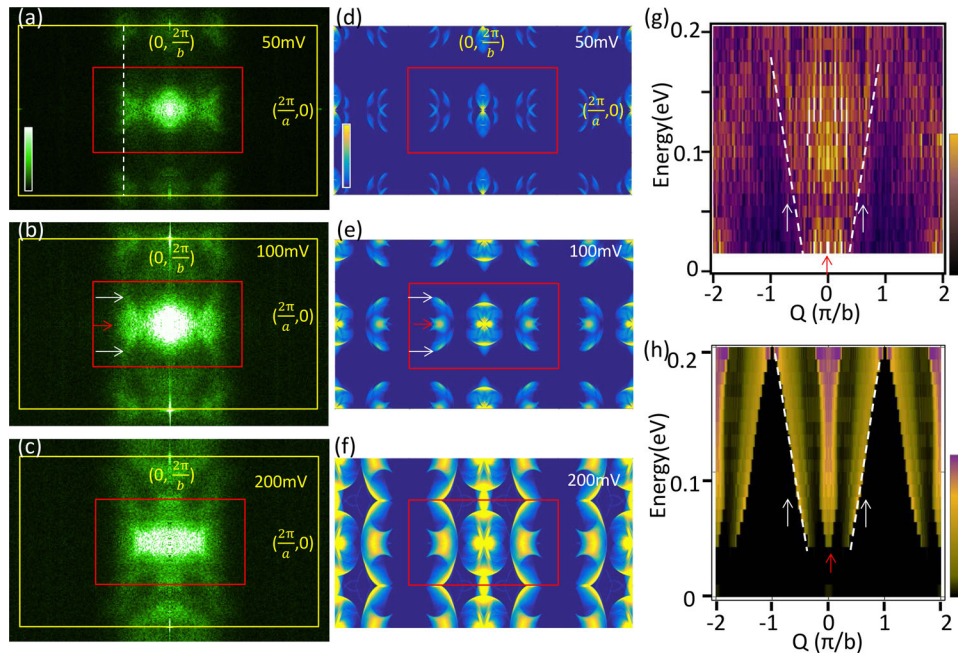


FIG. 3. [(a)–(c)] The experimental QPI maps taken at the indicated voltages. The areas inside red rectangles contain only features from intra-BZ scatterings. Bragg points $[(2\pi/a, 0)$ and $(0, 2\pi/b)]$ are marked on the images. [(d)–(f)] Theoretical QPI patterns derived from the surface-state-based calculations, which reasonably reproduce the features shown in the experimental data. In (b) and (e), white arrows point to the end points of the large crescent-shaped QPI contour while red arrows mark the small central features. [(g) and (h)] Experimental and theoretical E - Q dispersions taken along the dashed line in (a). The white dotted lines in (h) are drawn to mark the edges of the simulated feature and are placed in (g) as a guide to the eye. The white (red) arrow here indicates the strongly (weakly) dispersed QPI signals as marked by the corresponding white (red) arrows in (b) and (e).

Fermi arcs give clear interference signals. In a type-II Weyl semimetal, the large projected bulk pockets always appear in the surface CEC. In the calculated complete CEC at 50 meV of the $\text{Mo}_{0.66}\text{W}_{0.34}\text{Te}_2(001)$ surface, which includes both bulk and surface states as shown in Fig. 4(a), we plot two dominant scattering vectors, namely, \vec{Q}_1 connecting two electron pockets of the projected Weyl cone, and \vec{Q}_2 connecting the Weyl electron branch and the topologically trivial pocket at the \bar{Y} points. In the simulated QPI pattern [Fig. 4(b)], one can clearly distinguish the \vec{Q}_1 - and \vec{Q}_2 -induced features. But the simulated QPI map consists of seven pockets, more than what was observed in experiment (three pockets). Hence, it cannot be a correct interpretation of our observation. However, the situation is improved by removing the bulk bands and taking only the surface states into account [Fig. 4(c)]. The surface CEC is comprised only of two large semicircular-shaped contours and four small arclike pockets. The dominant scattering vectors are \vec{Q}_3 , which represents the scattering between two Fermi arc-derived surface contours, and \vec{Q}_4 , which links the

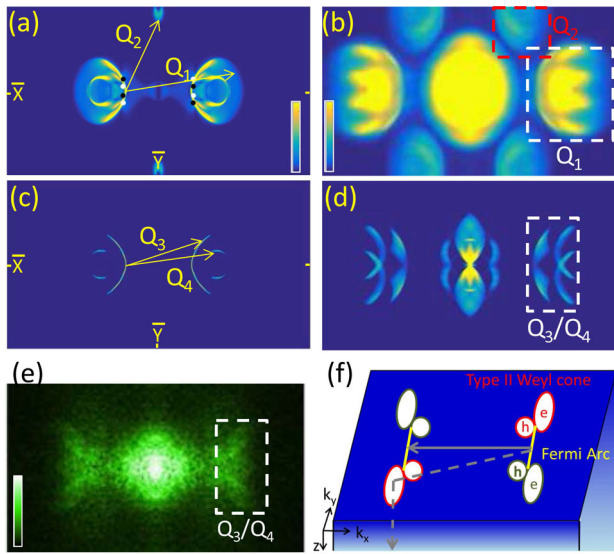


FIG. 4. (a) The calculated “complete” CEC that contains both bulk and surface state at $E = 50$ meV. (b) The QPI pattern based on (a), which presents only the intra-BZ scattering. (c) The calculated CEC with only surface states considered. The Fermi arc is the central segment of the semicircular contours. (d) The QPI pattern based on (b). (e) The experimental QPI data (50 mV). The white dotted rectangles in (d) and (e) are located in the same position in Q space and are the same size. (f) A cartoon demonstrating the sink effect of Weyl bulk states when the surface electron is scattered into a bulk pocket, a consequence of the topological bulk-surface connection. e (h) denotes the electron (hole) branch of a projected Weyl cone. Straight yellow lines represent the Fermi arcs. The solid arrow indicates the scattering between two surface Fermi arc states. The dotted arrow shows the process where an electron is scattered into one branch of a Weyl cone, and sinks into the bulk.

topological surface state to the trivial state. Both scattering processes involve the electrons in the Fermi arc. Therefore, the \vec{Q}_3 - and \vec{Q}_4 -derived QPI features inside the white rectangles in Fig. 4(d) serve as an explicit evidence of the QPI signal from Fermi arcs. In the QPI data in Fig. 4(e), we indeed observe these features. More importantly, the white rectangles in Figs. 4(d) and 4(e) are located in the same positions and are the same size. This proves that we have observed QPI pockets with comparable dimensions appearing at the predicted locations, providing more solid evidence of the detection of the Fermi arc in our experiment. The subtle differences in the fine QPI features may originate from the commonly used simple assumptions in the calculation [36]. We emphasize that because $\text{Mo}_x\text{W}_{1-x}\text{Te}_2$ has a simple band structure, the major feature of the surface-state-derived QPI pattern is robust. In addition, the agreement between our theory and experiment is remarkably good compared to previous QPI results on other materials.

Furthermore, comparison of the two simulations in Figs. 4(b) and 4(d) to the experimental data [Fig. 4(e)] suggests that the contribution of the bulk states to the QPI signal is negligible. This can be attributed to the difficulty of establishing an interference between a three-dimensional bulk electronic wave and a two-dimensional surface wave. In other words, when a surface electron, which initially occupies a state in the Fermi arc, is scattered by a point defect into a bulk state, it loses its surface character and diffuses into the bulk. In this sense, the bulk Weyl pocket behaves like a sink of surface electrons, which is a signature of the topological connection between a Weyl cone and Fermi arc [15,16,30]. On a type-I Weyl semimetal, the CEC at the energy of the Weyl point consists of a pointlike bulk state; therefore, the sinking effect is not prominent. By contrast, the type-II Weyl cones are heavily tilted, which gives rise to large areas of projected bulk pockets, and thus, this phenomenon should be more pronounced on a type-II Weyl semimetal surface.

In summary, we present theoretical QPI simulations and STM results on $\text{Mo}_x\text{W}_{1-x}\text{Te}_2$ illustrating its complex electronic structure for the first time, which are complementary to the recent ARPES measurements [37,38]. Our QPI measurements directly discern the topological Fermi arcs. Taken together, our calculations and experimental data suggest that the interference pattern is dominated by surface states, whereas the contribution from bulk states to QPI is negligible, indicating the topological connection between the Weyl bulk states and Fermi arc surface states. Our results on $\text{Mo}_x\text{W}_{1-x}\text{Te}_2$ establish a platform for further study of novel spectroscopic, optical, and transport phenomena that emerge in this compound.

H. Z., G. B., S.-Y. X., I. B., N. A., D. S. S., S. Z., and M. Z. H. are supported by the Gordon and Betty Moore Foundations EPIQS Initiative through Grant No. GBMF4547 and U.S. National Science Foundation (NSF) Grant

No. NSFDMR-1006492. H. Z. also acknowledges the support from the National Natural Science Foundation of China (Grant No. 11674226). G. C. and H. L. thank the National Research Foundation, Prime Ministers Office, Singapore, under its NRF fellowship (NRF Award No. NRF-NRFF2013-03). H. L., G. W., and S. J. are supported by the National Basic Research Program of China (Grants No. 2013CB921901 and No. 2014CB239302). N. Y. is supported in part by funding from the Princeton Center for Complex Materials, a MRSEC supported by NSF Grant No. DMR 1420541. T.-R. C. and H.-T. J. are supported by Ministry of Science and Technology, Academia Sinica, and National Tsing Hua University, Taiwan, and also thank NCHC, CINC-NTU, and NCTS, Taiwan, for technical support. F. S. acknowledges the National Key Projects for Basic Research of China (Grant No. 2013CB922103) and the National Natural Science Foundation of China (Grants No. 91421109, No. 11134005, and No. 11522432). A. B. is supported by the U.S. Department of Energy (DOE), Office of Science, Basic Energy Sciences Grant No. DE-FG02-07ER46352, and benefited from Northeastern University's Advanced Scientific Computation Center (ASCC) and the NERSC supercomputing center through DOE Award No. DE-AC02-05CH11231.

H. Z., G. B., and G. C. contributed equally to this work.

Note added.—Recently, we became aware of partial experimental STM data in a concomitant mainly-ARPES paper [39].

*mzhasan@princeton.edu

- [1] S. Murakami, *New J. Phys.* **9**, 356 (2007).
- [2] X. Wan, A. M. Turner, A. Vishwanath, and S. Y. Savrasov, *Phys. Rev. B* **83**, 205101 (2011).
- [3] L. Balents, *Physics* **4**, 36 (2011).
- [4] A. A. Burkov and L. Balents, *Phys. Rev. Lett.* **107**, 127205 (2011).
- [5] T. Ojanen, *Phys. Rev. B* **87**, 245112 (2013).
- [6] M. Z. Hasan, S.-Y. Xu, and G. Bian, *Phys. Scr.* **T164**, 014001 (2015).
- [7] A. M. Turner and A. Vishwanath, [arXiv:1301.0330](https://arxiv.org/abs/1301.0330).
- [8] S.-M. Huang, S.-Y. Xu, I. Belopolski, C.-C. Lee, G. Chang, B. Wang, N. Alidoust, G. Bian, M. Neupane, C. Zhang, S. Jia, A. Bansil, H. Lin, and M. Z. Hasan, *Nat. Commun.* **6**, 7373 (2015).
- [9] H. Weng, C. Fang, Z. Fang, B. A. Bernevig, and X. Dai, *Phys. Rev. X* **5**, 011029 (2015).
- [10] S.-Y. Xu, I. Belopolski, N. Alidoust, M. Neupane, G. Bian, C. Zhang, R. Sankar, G. Chang, Z. Yuan, C.-C. Lee, S.-M. Huang, H. Zheng, J. Ma, D. S. Sanchez, B. Wang, A. Bansil, F. Chou, P. P. Shibayev, H. Lin, S. Jia, and M. Z. Hasan, *Science* **349**, 613 (2015).
- [11] B. Q. Lv, H. M. Weng, B. B. Fu, X. P. Wang, H. Miao, J. Ma, P. Richard, X. C. Huang, L. X. Zhao, G. F. Chen, Z. Fang, X. Dai, T. Qian, and H. Ding, *Phys. Rev. X* **5**, 031013 (2015).
- [12] X. Huang, L. Zhao, Y. Long, P. Wang, D. Chen, Z. Yang, H. Liang, M. Xue, H. Weng, Z. Fang, X. Dai, and G. Chen, *Phys. Rev. X* **5**, 031023 (2015).
- [13] C.-L. Zhang, S.-Y. Xu, I. Belopolski, Z. Yuan, Z. Lin, B. Tong, G. Bian, N. Alidoust, C.-C. Lee, S.-M. Huang, T.-R. Chang, G. Chang, C.-H. Hsu, H.-T. Jeng, M. Neupane, D. S. Sanchez, H. Zheng, J. Wang, H. Lin, C. Zhang, H.-Z. Lu, S.-Q. Shen, T. Neupert, M. Z. Hasan, and S. Jia, *Nat. Commun.* **7**, 10735 (2015).
- [14] H. Zheng, S.-Y. Xu, G. Bian, C. Guo, G. Chang, D. S. Sanchez, I. Belopolski, C.-C. Lee, S.-M. Huang, X. Zhang, R. Sankar, N. Alidoust, T.-R. Chang, F. Wu, T. Neupert, F. Chou, H.-T. Jeng, N. Yao, A. Bansil, S. Jia, H. Lin, and M. Z. Hasan, *ACS Nano* **10**, 1378 (2016).
- [15] H. Inoue, A. Gyenis, Z. Wang, J. Li, S. W. Oh, S. Jiang, N. Ni, B. A. Bernevig, and A. Yazdani, *Science* **351**, 1184 (2016).
- [16] R. Batabyal, N. Morali, N. Avraham, Y. Sun, M. Schmidt, C. Felser, A. Stern, B. Yan, and H. Beidenkopf, *Sci. Adv.* **2**, e1600709 (2016).
- [17] P. Sessi, Y. Sun, T. Bathon, F. Glott, Z. Li, H. Chen, L. Guo, X. Chen, M. Schmidt, C. Felser, B. Yan, and M. Bode, [arXiv:1606.00243](https://arxiv.org/abs/1606.00243).
- [18] A. A. Soluyanov, D. Gresch, Z. Wang, Q. Wu, M. Troyer, X. Dai, and B. A. Bernevig, *Nature (London)* **527**, 495 (2015).
- [19] Y. Sun, S.-C. Wu, M. N. Ali, C. Felser, and B. Yan, *Phys. Rev. B* **92**, 161107 (2015).
- [20] T.-R. Chang, S.-Y. Xu, G. Chang, C.-C. Lee, S.-M. Huang, B. Wang, G. Bian, H. Zheng, D. S. Sanchez, I. Belopolski, N. Alidoust, M. Neupane, A. Bansil, H.-T. Jeng, H. Lin, and M. Z. Hasan, *Nat. Commun.* **7**, 10639 (2016).
- [21] Z. Wang, D. Gresch, A. A. Soluyanov, W. Xie, S. Kushwaha, X. Dai, M. Troyer, R. J. Cava, and B. A. Bernevig, *Phys. Rev. Lett.* **117**, 056805 (2016).
- [22] A. G. Grushin, *Phys. Rev. D* **86**, 045001 (2012).
- [23] A. A. Zyuzin and R. P. Tiwari, *JETP Lett.* **103**, 717 (2016).
- [24] H. Isobe and N. Nagaosa, *Phys. Rev. Lett.* **116**, 116803 (2016).
- [25] P. Roushan, J. Seo, C. V. Parker, Y. S. Hor, D. Hsieh, D. Qian, A. Richardella, M. Z. Hasan, R. J. Cava, and A. Yazdani, *Nature (London)* **460**, 1106 (2009).
- [26] T. Zhang, P. Cheng, X. Chen, J.-F. Jia, X. Ma, K. He, L. Wang, H. Zhang, X. Dai, Z. Fang, X. Xie, and Q.-K. Xue, *Phys. Rev. Lett.* **103**, 266803 (2009).
- [27] I. Lee, C. K. Kim, J. Lee, S. J. L. Billinge, R. Zhong, J. A. Schneeloch, T. Liu, T. Valla, J. M. Tranquada, G. Gu, and J. C. S. Davis, *Proc. Natl. Acad. Sci. U.S.A.* **112**, 1316 (2015).
- [28] I. Zeljkovic, Y. Okada, C.-Y. Huang, R. Sankar, D. Walkup, W. Zhou, M. Serbyn, F. Chou, W.-F. Tsai, H. Lin, A. Bansil, L. Fu, M. Z. Hasan, and V. Madhavan, *Nat. Phys.* **10**, 572 (2014).
- [29] D. Zhang, H. Baek, J. Ha, T. Zhang, J. Wyrick, A. V. Davydov, Y. Kuk, and J. A. Stroscio, *Phys. Rev. B* **89**, 245445 (2014).
- [30] A. C. Potter, I. Kimchi, and A. Vishwanath, *Nat. Commun.* **5**, 5161 (2014).
- [31] P. Hosur, *Phys. Rev. B* **86**, 195102 (2012).
- [32] G. Chang, S.-Y. Xu, H. Zheng, C.-C. Lee, S.-M. Huang, I. Belopolski, D. S. Sanchez, G. Bian, N. Alidoust, T.-R. Chang, C.-H. Hsu, H.-T. Jeng, A. Bansil, H. Lin, and M. Z. Hasan, *Phys. Rev. Lett.* **116**, 066601 (2016).

- [33] A. K. Mitchell and L. Fritz, *Phys. Rev. B* **93**, 035137 (2016).
- [40] G. Kresse and J. Furthmüller, *Phys. Rev. B* **54**, 11169 (1996).
- [41] N. Marzari and D. Vanderbilt, *Phys. Rev. B* **56**, 12847 (1997).
- [42] D. E. P. Vanpoucke and G. Brocks, *Phys. Rev. B* **77**, 241308 (2008).
- [34] See Supplemental Material at <http://link.aps.org/supplemental/10.1103/PhysRevLett.117.266804> for the detailed description of the calculation method and more experimental QPI maps.
- [35] B. Brown, *Acta Crystallogr.* **20**, 268 (1966).
- [36] To simulate a QPI pattern in Q space, it is a common practice to calculate the joint density of states with restrictions from spin and/or orbital textures. The simulation is simplified by considering the point defect as a δ -function, by ignoring the shape of its wave function, and scattering anisotropy of the defect. Though it may cause some minor discrepancy in the fine structures, it is widely accepted that the simulation is capable of capturing all dominated QPI features (the number, positions, and sizes of QPI pockets).
- [37] I. Belopolski, S.-Y. Xu, Y. Ishida, X. Pan, P. Yu, D. S. Sanchez, H. Zheng, M. Neupane, N. Alidoust, G. Chang, T.-R. Chang, Y. Wu, G. Bian, S.-M. Huang, C.-C. Lee, D. Mou, L. Huang, Y. Song, B. Wang, G. Wang, Y.-W. Yeh, N. Yao, J. E. Rault, P. Le Fevre, F. Bertran, H.-T. Jeng, T. Kondo, A. Kaminski, H. Lin, Z. Liu, F. Song, S. Shin, and M. Z. Hasan, *Phys. Rev. B* **94**, 085127 (2016).
- [38] A. Tamai, Q. S. Wu, I. Cucchi, F. Y. Bruno, S. Ricco, T. K. Kim, M. Hoesch, C. Barreteau, E. Giannini, C. Besnard, A. A. Soluyanov, and F. Baumberger, *Phys. Rev. X* **6**, 031021 (2016).
- [39] K. Deng, G. Wan, P. Deng, K. Zhang, S. Ding, E. Wang, M. Yan, H. Huang, H. Zhang, Z. Xu, J. Denlinger, A. Fedorov, H. Yang, W. Duan, H. Yao, Y. Wu, S. Fan, H. Zhang, X. Chen, and S. Zhou, *Nat. Phys.* **12**, 1105 (2016).